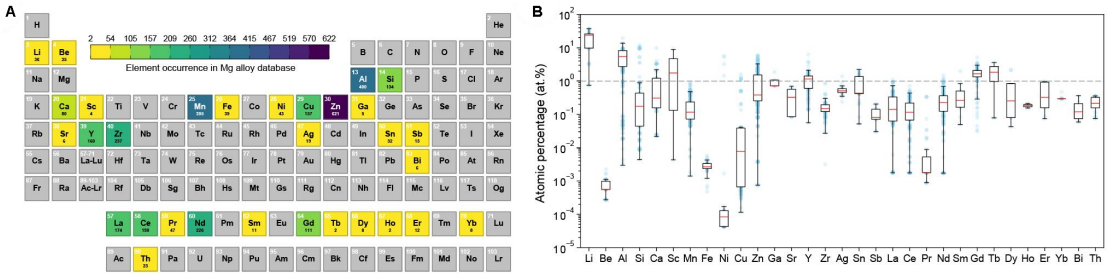
Supplementary Materials

Chemical similarity description of liquid kinetics across composition space in magnesium alloys

Jiang You[1], Cheng Wang[2,*], Hui-Yuan Wang[2]

[1]College of Materials Science and Engineering, Taiyuan University of Technology, Taiyuan 030024, Shanxi, China.
[2]National Key Laboratory of Automotive Chassis Integration and Bionics & School of Materials Science and Engineering, Jilin University, Changchun 130025, Jilin, China.

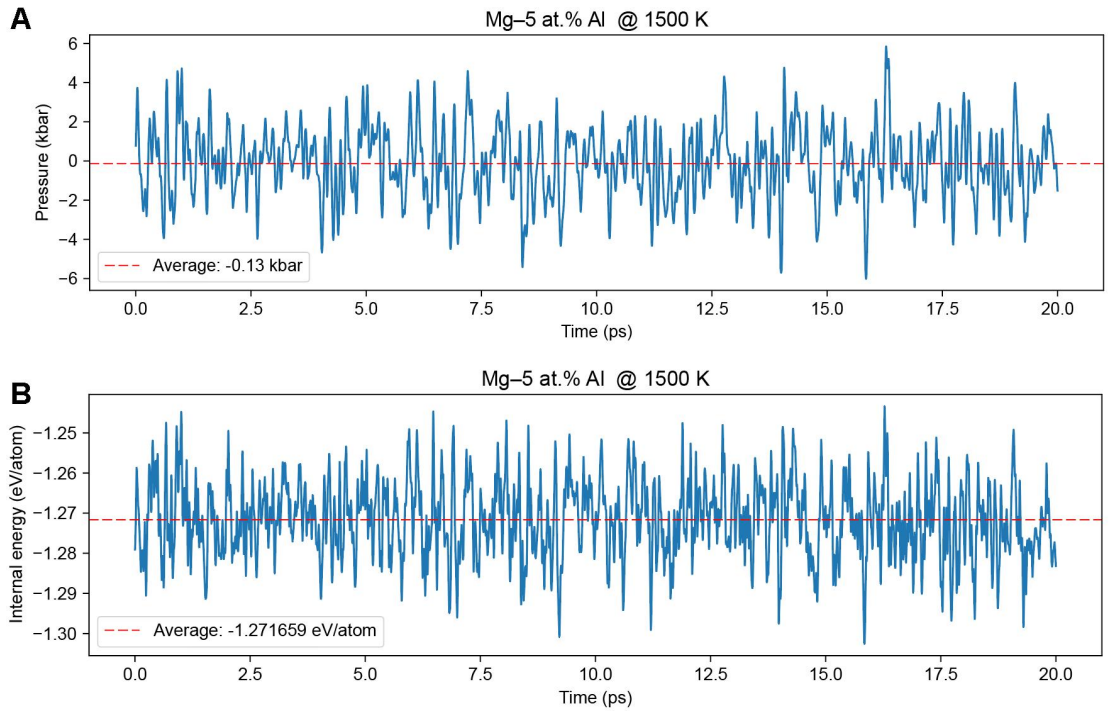
[*]**Correspondence to:** Prof. Cheng Wang, National Key Laboratory of Automotive Chassis Integration and Bionics & School of Materials Science and Engineering, Jilin University, Changchun 130025, Jilin, China. E-mail: chengwang@jlu.edu.cn



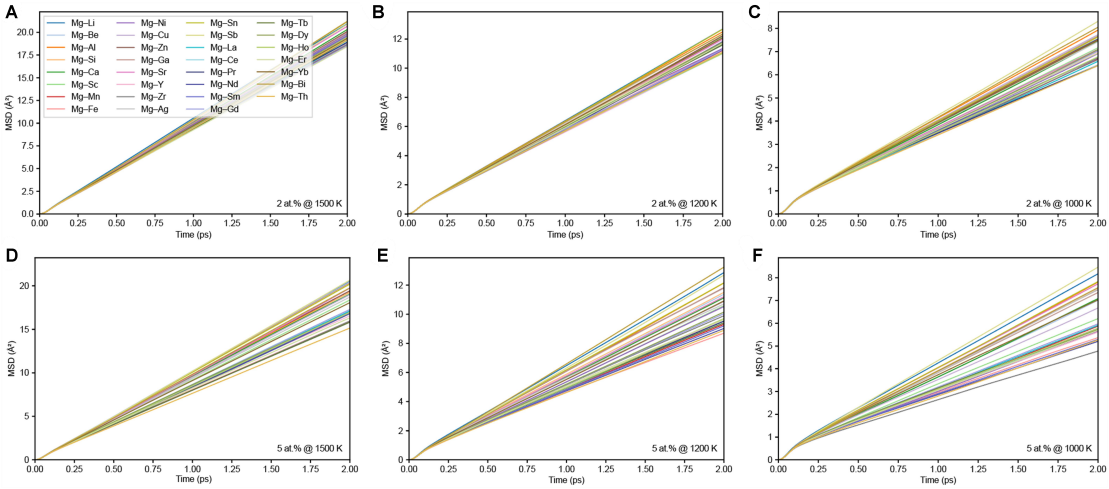
Supplementary Figure 1. (A) Periodic table illustrating the 31 solute elements in Mg alloys, with color intensity corresponding to their occurrence frequency in the Mg alloy database. (B) Box plot of atomic percentages for each solute element across all alloy compositions in the database. The box spans the interquartile range (25th–75th percentile), the red line indicates the median, and the whiskers extend to the most extreme data points within 1.5× the interquartile range. The individual data points are overlaid as blue markers. Sample sizes (in the order of the elements shown on the x-axis): 36, 35, 400, 134, 80, 4, 395, 39, 43, 157, 621, 5, 6, 160, 237, 19, 32, 13, 174, 190, 47, 226, 11, 111, 2, 8, 2, 12, 8, 6, 23.

To ensure that the composition space investigated in our AIMD simulations is representative of practical engineering Mg alloys, we refer a comprehensive open-source Mg alloy database compiled from the experimental studies [1]. The database includes a total of 31 solute elements: Li, Be, Al, Si, Ca, Sc, Mn, Fe, Ni, Cu, Zn, Ga, Sr, Y, Zr, Ag, Sn, Sb, Bi, La, Ce, Pr, Nd, Sm, Gd, Tb, Dy, Ho, Er, Yb, and Th. Supplementary Figure 1A highlights these solute elements on the periodic table, with color intensity reflecting their frequency of occurrence across all documented alloy compositions in the database. The most commonly emloyed solutes are Zn, Mn, and Al, while rare-earth elements collectively exhibit significant prevalence.

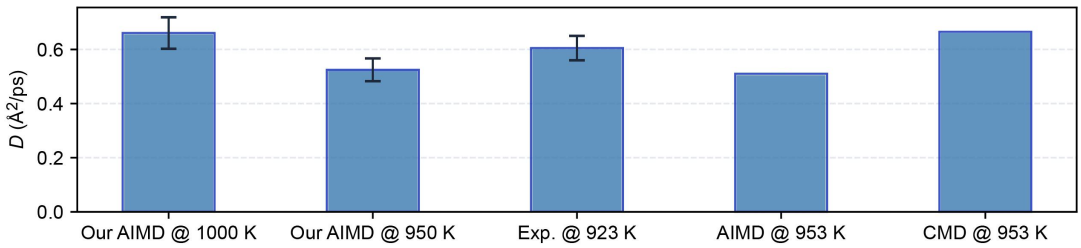
Supplementary Figure 1B presents box plots of the atomic percentages (at. %) for each solute element across the entire database. Each box plot illustrates the statistical distribution: the central red line indicates the median concentration, the box spans the interquartile range (from the 25th to 75th percentile), whiskers extend to the most extreme data points within 1.5 times the interquartile range, and individual outliers are marked as points. It is clear that solute concentrations in Mg alloys are predominantly low, a characteristic feature of Mg alloy design aimed at preserving low density while improving strength, corrosion resistance, or other properties. Medians for most solute elements are below 5 at. %, and consequently, we focus on the 31 solute elements listed above at two dilute concentrations: 2 at. % and 5 at. %.



Supplementary Figure 2. The time evolution of (A) pressure and (B) internal energy for the Mg–5 at. % Al liquid alloys at 1500 K.



Supplementary Figure 3. The MSD curves for binary Mg liquid alloys at solute concentrations of 2 at.% and 5 at.%, and temperatures of 1500 K, 1200 K, and 1000 K. (A-C) show the MSD curves at a solute concentration of 2 at.% for 1500 K, 1200 K, and 1000 K, respectively; (D-F) show the corresponding curves at 5 at.%.



Supplementary Figure 4. Diffusion coefficient of liquid Mg obtained in the present AIMD simulations compared with experimental measurements [2,3] and previously reported AIMD [4] and classical MD results [5]. The error bar represent the standard deviation.

To rigorously evaluate the influence of finite-size effects and simulation time on the calculated diffusion coefficients, we performed large-scale molecular dynamics simulations using the Deep Potential (DP) framework [6]. We employ the Potential-Smooth Edition of the DeePMD-kit package [6] to train the DPs, which involves the mapping of local atomic configuration to atomic energy by a deep neural network [7]. The total energy of system is then determined as the sum of atomic energies. The relative coordinates R^i are converted to the generalized coordinates $\widetilde{R}^i$:

$$\{R_i\}=\{x_{ji},y_{ji},z_{ji}\}\rightarrow\{\widetilde{R}^i\}=\{s(r_{ji}),\tilde{x}_{ji},\tilde{y}_{ji},\tilde{z}_{ji}\} \quad (1)$$

where $\tilde{x}_{ji}=\frac{s(r_{ji})x_{ji}}{r_{ji}},\tilde{y}_{ji}=\frac{s(r_{ji})y_{ji}}{r_{ji}},\tilde{z}_{ji}=\frac{s(r_{ji})z_{ji}}{r_{ji}}$, and contains angular information. $s(r_{ji})$ is a continuous and differentiable scalar weighting function containing radial information, defined as:

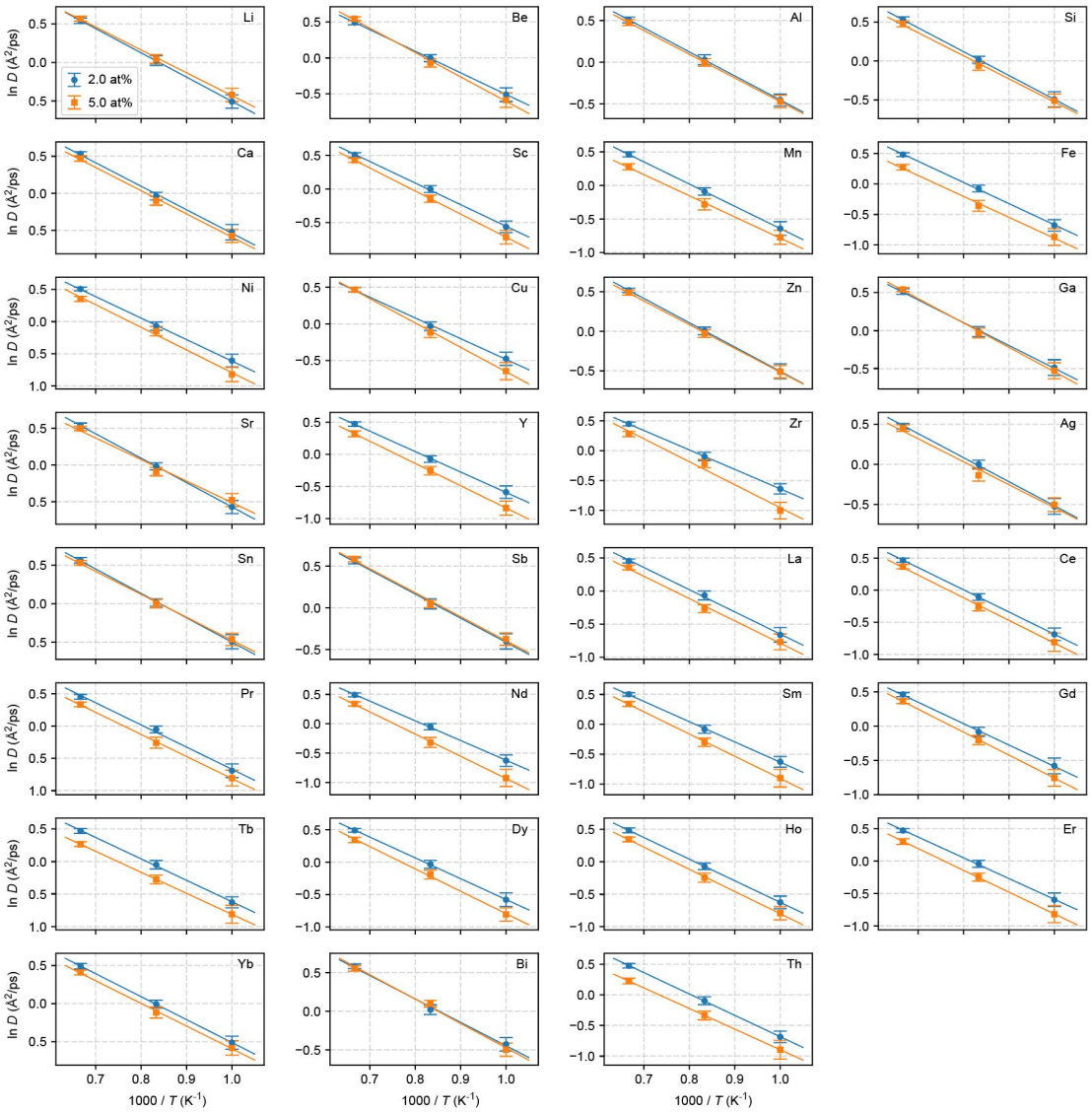
$$s(r_{ji})=\begin{cases}\dfrac{1}{r_{ji}}, & r_{ji}<r_{cs}\\ \dfrac{1}{r_{ji}}\left[x^3(-6x^2+15x-10)+1\right], & r_{cs}<r_{ji}<r_c\\ 0, & r_{ji}>r_c\end{cases} \quad (2)$$

where $x=\frac{r_{ji}-r_{cs}}{r_c-r_{cs}}$. The smooth cutoff r_{cs} is set as 6.8 Å. The radial cutoff r_c is taken as 7.0 Å. The embedding neural network is {25, 50, 100} with three hidden layers. The fitting neural network has three hidden layers with 240 neurons per layer to yield the atomic energy. The number of training steps is 3,000,000. The exponentially decaying learning rate is used with the Adam optimizer. The initial learning rate, decay step, and final learning rate are 0.001, 10000, and 1×10^{-8}, respectively. The loss function is defined as:

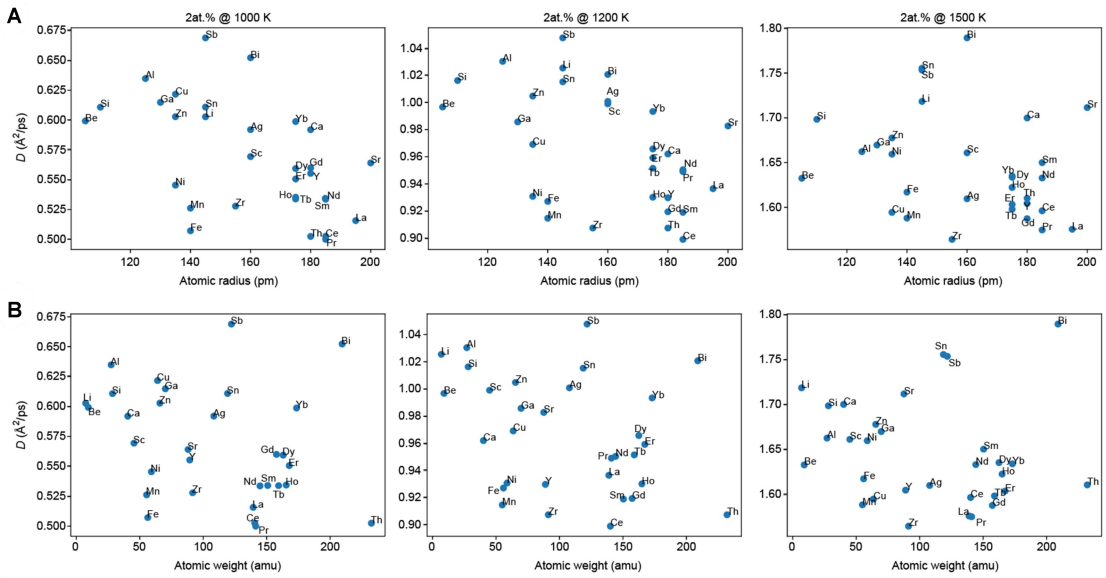
$$L(p_E, p_F)=p_E\Delta E^2+\frac{p_F}{3N}\sum_i |\Delta F_i|^2 \quad (3)$$

where ΔE and ΔF_i are energy and force differences per atom between the neural network prediction and the *ab-initio* data, and N is the number of atoms. To minimize the loss function in a well-balanced way [7], the p_E varies from 0.01 to 1 and the p_F starts at 1000 and ends at 1.

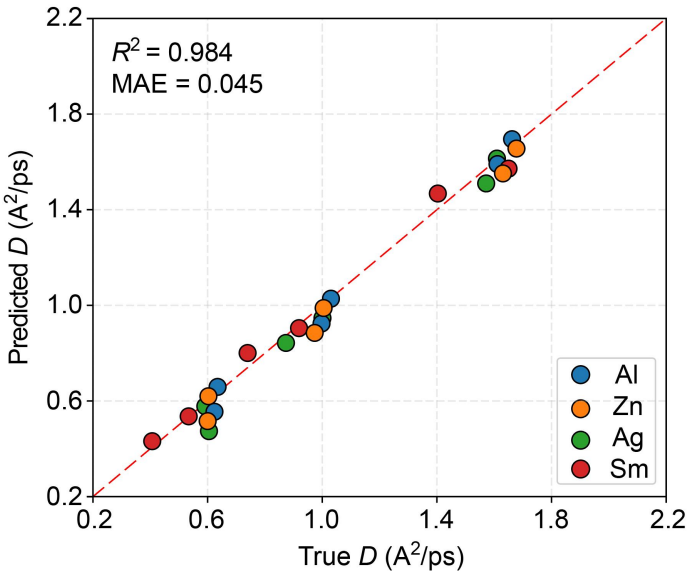
In DPMD simulations, to ensure structural ergodicity and eliminate memory effects from the initial setup, each system underwent an extensive thermalization protocol. Each system was first relaxed for 2 ns and followed by quenching in NPT ensemble. The collected configurations are further relaxed for 1 ns in NPT ensemble and switched to NVT ensemble for another 1 ns to produce statistical analysis. The timestep is set as 2 fs and the temperature is controlled by the Nose-Hoover thermostat. We performed large-scale DPMD simulations on the Mg–5 at.% Al system, spanning both extended spatial and temporal scales. By replicating the AIMD-relaxed supercells into configurations containing up to 12,800 atoms (4×4×4 expansion), we directly compared the convergence of D across various system sizes.



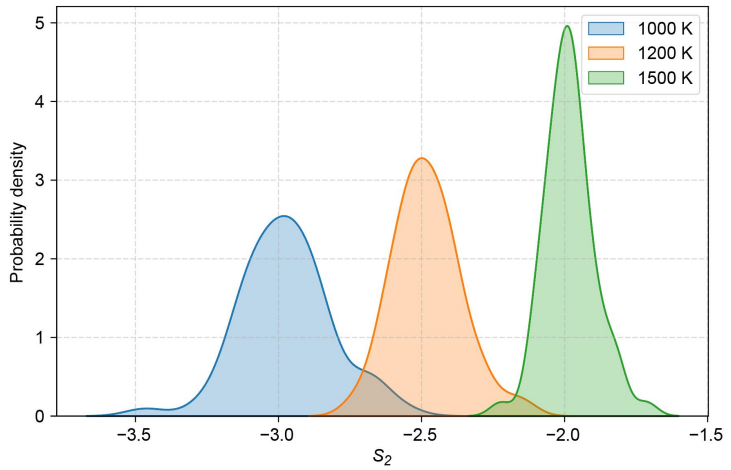
Supplementary Figure 5. Arrhenius fits of the diffusion coefficients for each binary Mg liquid alloys. The error bar represent the standard deviation.



Supplementary Figure 6. Correlations between diffusion coefficient and (A) atomic radius and (B) atomic weight for binary Mg liquid alloys at the investigated concentrations and temperatures.

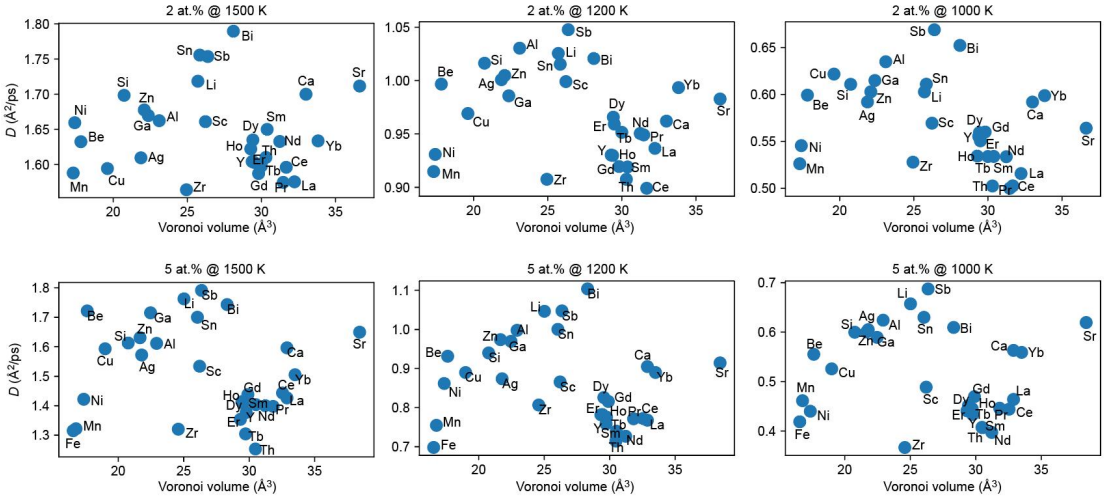


Supplementary Figure 7. Hold-out validation of the predictive capability of the chemical similarity description model. Al, Zn, Ag, and Sm were excluded from parameter fitting and subsequently predicted.

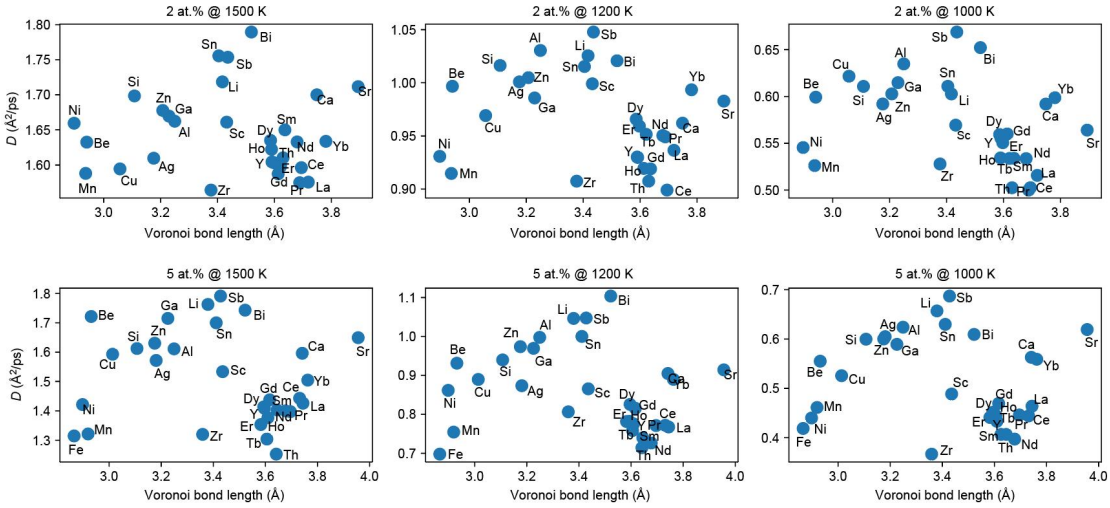


Supplementary Figure 8. Probability densities of S_2 for the investigated binary Mg liquid alloys at temperatures 1500 K, 1200 K and 1000 K.

The probability densities of the two-body entropy S_2 provide a statistical measure of the local structural order in liquid alloys. For the investigated binary Mg-based liquid alloys, the distributions of S_2 were evaluated at three representative temperatures: 1500 K, 1200 K, and 1000 K. At 1500 K, the S_2 distributions are relatively narrow and centered around lower negative values, indicating a predominantly disordered liquid structure with weak short-range correlations. As the temperature decreases to 1200 K, the distributions shift toward more negative S_2 values and slightly broaden, reflecting the gradual development of short-range order in the liquid. At the lowest temperature of 1000 K, the probability densities become even broader and exhibit more pronounced tails, suggesting that significant local structural heterogeneities emerge as the system approaches the undercooled regime.

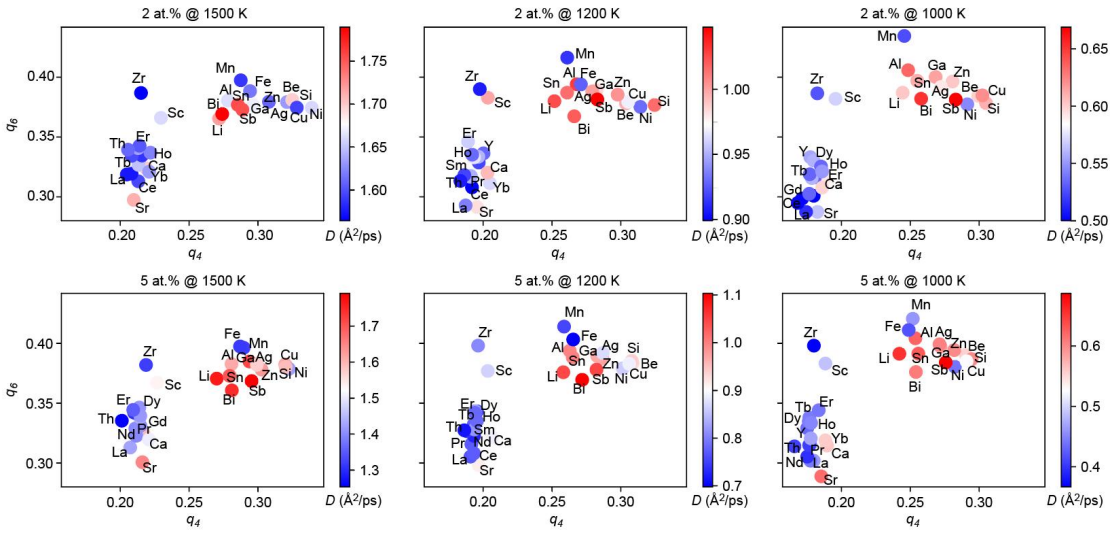


Supplementary Figure 9. Correlation between Voronoi volume and diffusion coefficient for corresponding binary Mg liquid alloys at the investigated concentrations and temperatures.



Supplementary Figure 10. Correlation between Voronoi bond length and diffusion coefficient for corresponding binary Mg liquid alloys at the investigated concentrations and temperatures.

The atomic Voronoi volume and bond length are evaluated based on the Voronoi tessellation [8]. Note that small faces less than 2% threshold of total face area are removed to eliminate numerical noise due to small perturbations of the atomic positions.



Supplementary Figure 11. Correlation between q_4-q_6 map and diffusion coefficient for corresponding binary Mg liquid alloys at the investigated concentrations and temperatures.

To calculate the bond orientational order [9], a $2l+1$ vector of the l-fold symmetry for atom i is first computed as

$$q_{lm}(i)=\frac{1}{N_i}\sum_{j=1}^{N_i} Y_{lm}\left(\theta(\boldsymbol{r_{ij}}),\phi(\boldsymbol{r_{ij}})\right) \tag{4}$$

where m are integers from $-l$ to l, and Y_{lm} is the spherical harmonics. Then q_l is calculated as

$$q_l=\sqrt{\frac{4\pi}{2l+1}\sum_{m=-l}^{l}|q_{lm}|^2} \tag{5}$$

REFERENCES

[1] M. Ghorbani, M. Boley, P.N.H. Nakashima, N. Birbilis, A machine learning approach for accelerated design of magnesium alloys . Part A : Alloy data and property space, J. Magnes. Alloy. 11 (2023) 3620–3633. https://doi.org/10.1016/j.jma.2023.09.035.

[2] T. IIDA, R.I.L. Guthrie, The physical properties of liquid metals, Clarendon press OXFORD, 1986.

[3] T. Iida, R. Guthrie, N. Tripathi, A Model for Accurate Predictions of Self-Diffusivities in Liquid Metals , Semimetals , and Semiconductors, Metall. Mater. Trans. B 37 (2006) 559–564.

[4] S. Sengul, D.J. Gonzalez, L.E. Gonzalez, Structural and dynamical properties of liquid Mg . An orbital-free molecular, J. Phys. Condens. MATTER 21 (2009) 115106. https://doi.org/10.1088/0953-8984/21/11/115106.

[5] L.J. Gallego, M.M.G. Alemany, J. Casas, C. Rey, L.E. Gonza, Dynamic properties of liquid alkaline-earth metals, Phys. Rev. E 56 (1997) 6818–6828.

[6] H. Wang, L. Zhang, J. Han, W. E, DeePMD-kit: A deep learning package for many-body potential energy representation and molecular dynamics, Comput. Phys. Commun. 228 (2018) 178–184. https://doi.org/10.1016/j.cpc.2018.03.016.

[7] L. Zhang, J. Han, H. Wang, R. Car, E. Weinan, Deep Potential Molecular Dynamics: A Scalable Model with the Accuracy of Quantum Mechanics, Phys. Rev. Lett. 120 (2018) 143001. https://doi.org/10.1103/PhysRevLett.120.143001.

[8] J. You, C. Wang, S. Shang, Y. Gao, H. Ju, H. Ning, Y. Wang, H.Y. Wang, Z.K. Liu, Ordering in liquid and its heredity impact on phase transformation of Mg-Al-Ca alloys, J. Magnes. Alloy. 11 (2023) 2006–2017. https://doi.org/10.1016/j.jma.2021.11.024.

[9] S. Ishino, Y.C. Hu, H. Tanaka, Microscopic structural origin of slow dynamics in glass-forming liquids, Nat. Mater. 24 (2025) 268–277. https://doi.org/10.1038/s41563-024-02068-8.